Supplementary Information

Benign methylformamidinium byproduct induced by cation heterogeneity inhibits local formation of δ-phase perovskites

Jihoo Lim[1†], Jaehui Kim[2†], Josh Davies-Jones[3], Mohsen Danaie[4], Eunyoung Choi[4,5], Hongjae Shim[1], Liang Chen[2], Jincheol Kim[6], Judy S. Kim[7], Philip R. Davies[3], Jan Seidel[8,9], Martin A. Green[1], Samuel D. Stranks[5], Sang Il Seok[2*], Jae Sung Yun[1,10*]

[1]Australian Centre for Advanced Photovoltaics (ACAP), School of Photovoltaic and Renewable Energy Engineering, University of New South Wales, Sydney, NSW 2052, Australia

[2]Department of Energy and Chemical Engineering, Ulsan National Institute of Science and Technology (UNIST), 50 UNIST-Gil, Eonyang-eup, Ulju-gun, Ulsan 44919, Republic of Korea

[3]Cardiff Catalysis Institute, School of Chemistry, Cardiff University, Cardiff, CF10 3AT, United Kingdom

[4]Diamond Light Source Ltd, Harwell Science and Innovation Campus, Didcot, OX11 0DE, United Kingdom

[5]Department of Chemical Engineering and Biotechnology, University of Cambridge, Philippa Fawcett Drive, Cambridge CB3 0AS, United Kingdom

[6]Sustainable Energy Research Centre, School of Engineering, Macquarie University, Sydney, NSW 2109, Australia

[7]Department of Materials, University of Oxford, Oxford, OX1 3PH, United Kingdom

[8]School of Materials Science and Engineering, University of New South Wales, Sydney, NSW 2052, Australia

[9]ARC Centre of Excellence in Future Low-Energy Electronics Technologies (FLEET), University of New South Wales, Sydney, NSW 2052, Australia

[10]Department of Electrical and Electronic Engineering, Advanced Technology Institute (ATI), University of Surrey, Guildford GU2 7XH, United Kingdom

*Corresponding authors. E-mail: seoksi@unist.ac.kr and j.yun@surrey.ac.uk

†These authors contributed equally to this work.

Experimental Section

Materials:

The Chemicals were purchased from the following information: Formamidinium iodide (FAI; 99.99%, GreatCell Solar), lead(II) iodide (PbI_2; 99.99%, TCI), methylammonium chloride (MACl; Merck), 4-methoxy-phenethylammonium iodide (MeO-PEAI; 99%, GreatCell Solar), N,N-dimethylformamide (DMF; anhydrous, 99.8%, Sigma-Aldrich), dimethyl sulfoxide (DMSO; anhydrous, 99.9%, Sigma-Aldrich), 2-propanol (anhydrous, 99.5%, Sigma-Aldrich), 2-methoxyethanol (2-ME; anhydrous, 99.8%, Sigma-Aldrich), chlorobenzene (anhydrous, 99.8%, Sigma-Aldrich), acetonitrile (ACN; anhydrous, 99.8%, Sigma-Aldrich), Spiro-OMeTAD (Lumtec), 4-tert-butylpyridine (t-BP; 98%, Sigma-Aldrich), bis(trifluoromethane)sulfonimide lithium salt (Li-TFSI; 99.95%, Sigma-Aldrich), FK209 Co(III) TFSI salt (Lumtec) and ethyl ether (99.0%, SAMCHUN).

$FAPbI_3$ black powder

FAI and PbI_2 were dissolved in 2-ME in a 1:1 molar ratio. After stirring the solution for 20 minutes at room temperature, it was stirred at 120 °C for over 45 min. The black $FAPbI_3$ powders were vacuum-filtered and then dried at 150 °C for 30 minutes.

Device fabrication:

$FAPbI_3$ perovskite solar cells were fabricated with the following procedure. FTO glass (Asahi VU glass, 12–13 Ω cm^{-2}) substrates were sonicated in detergent, DI water, acetone and then ethanol for 20 min each. The hole blocking TiO_2 (bl-TiO_2) layer was coated on the FTO through the spray pyrolysis deposition of 20Mm titanium diisopropoxide bis(acetylacetonate) in ethanol (99.9%) at 450 °C. Mesoporous TiO_2 (mp-TiO_2) was further topped via spin-coating at 1,500 rpm for 40 s on the substrate with TiO_2 paste (Sharechem) dispersed in 2ME/terpineol solvent (3.5:1 w/w). The substrate underwent sintering process at 500 °C for 1 h. The perovskite precursor solutions were prepared by dissolving 1.4 M $FAPbI_3$ powder with MACl (0, 15, 50, and 80 mol%) in a mixed solvent of DMF:DMSO = 8:1. The solutions were stirred at 60 °C for 20 min. The perovskite solutions were then spin-coated onto the substrate at 500 rpm for 5 s, 1,000 rpm for 5 s and 5,000 rpm for 17 s; ethyl ether 1 mL was dropped over the substrate at 8-9 s during 5000 rpm spinning. The spin-coated perovskite films were annealed at 150 °C for 15 min, and then 100 °C for 15 min. To passivate surface defects, MeO-PEAI solution (4 mg/mL IPA) was spin-coated at 5,000 rpm for 30 s and annealed at 100 °C for 5 min (Please note that MeO-PEAI was deposited only for device fabrication and characterisation in **Figure S5-6**). The spiro-OMeTAD solution was prepared by the mixture of 94 mg in 1.1 mL chlorobenzene with 37 μL t-BP, 23 μL Li-TFSI (520 mg mL^{-1} in ACN), and 9 μL Co-TFSI salt (375 mg mL^{-1} in ACN) were spin-coated at 3,500 rpm for 30 s. A 80 nm thick gold was deposited via thermal evaporation.

Characterisation:

Photo-induced Force Microscopy (PiFM):

PiFM data were obtained under ambient conditions using a VistaScope AFM platform manufactured by Molecular Vista (San Jose, CA, USA) exploiting a QCL laser (760 - 1860 cm^{-1}). The technique provides simultaneous topographic and vibrational spectroscopy information. In the experiments reported here, the sample was mapped at 1713 cm^{-1} and 1610 cm^{-1}, which arise from C-N stretching band of the formamidinium, and partial C=N bonding of methylformamidinium cation, respectively. The “bulk” region was scanned with direct detection mode which samples a depth of up to ~300 nm, where the cantilever is actuated at its primary resonance frequency v_1, while the repetition rate of the stimulating laser is adjusted to correspond to the secondary resonance frequency v_2, whereas the “surface” region was scanned using sideband mode detection which samples a depth of ~ 20- 30 nm,

wherein the second driving force is modulated to a 'beat' frequency, which corresponds to the difference or sum of the two mechanical resonances as v_1-v_2 (or v_1+v_2).

Current density-voltage (*J-V*) measurement:

The *J–V* characteristics of the devices were measured using a Keithley 2420 source meter under illumination by a solar simulator (Newport, Oriel Sol3A class AAA) with an AM 1.5 G filter and 100 mW cm^{-2} irradiation intensity. The active area was shaped by a metal mask in front of the solar cell to avoid the overestimation of the photocurrent density. A spectral mismatch factor of 1.05 was used for all *J–V* measurements. For the measurement of high-efficiency devices, an antireflective film (NanoEcoWay Co., Ltd.) was applied to the surface.

Proton nuclear magnetic resonance spectroscopy (^{1}H-NMR):

Solution and film NMR spectra were performed with a 400 MHz FT-NMR (Bruker, AVANCE III HD) spectrometer equipped 5 mm BBO probe. ^{1}H spectra were recorded using zg30 pulse with recycle delay of 17 s, 90° pulse width of 10 μs, and acquisition time of 4.0894 s to the resonance frequency of 400.22 MHz. The total number of scans was 32. The chemical shift is referenced to a DMSO-D6 at ^{1}H (2.5 ppm).

Four-dimensional Scanning Transmission Electron Microscopy (4D-STEM):

Four-dimensional scanning transmission electron microscopy (4D-STEM) measurements were acquired on a JEOL ARM300CF (E02) at the Electron Physical Science Imaging Centre (ePSIC), Diamond Light Source using a MerlinEM direct electron detector. With the probe corrector optics turned off, we aligned the microscope to minimise the probe convergence semi-angle for better Bragg peaks visibility in diffraction patterns. Experimental parameters are as follows: 300 kV of accelerating voltage; 20 cm of camera length; 20 msec of Dwell time; 80kX of magnification. Standard evaporated gold nanoparticles on amorphous carbon were used for collecting calibration data. Acquired datasets were analysed by customised notebook based on py4DSTEM and HyperSpy packages.

Wavelength-dependent Kelvin probe force microscopy (KPFM):

All KPFM measurements were carried out using a commercial AFM system (AIST-NT smartSPM1000) under N_2 condition at room temperature. Before the measurement, possible contaminants on the surface of the sample were blown away using a nitrogen gun. The platinum AFM tip (HQ:NSC35/Pt) was used. First, CPD spatial maps of samples were obtained in dark condition. Subsequently, an external tunable light source (FemtoPower 1060, NKT photonics Inc.) with a pulse width of 200 fs, a high-repetition-rate of 80 MHz, and a bandwidth of 25 nm was used to illuminate the samples at an angle of 30° to the surface to avoid shading caused by the AFM probe. The wavelength of 400 and 800 nm with the power intensity of 15 uW was used. Both the wavelength and intensity of the light source were controllable.

Steady-state spectral photoluminescence (PL) measurement:

Steady-state PL was measured using a commercial time-correlated single-photon-counting setup (FluoTime 300, PicoQuant GmbH) equipped with a PMA-C-192-M detector and high-resolution excitation monochromators.

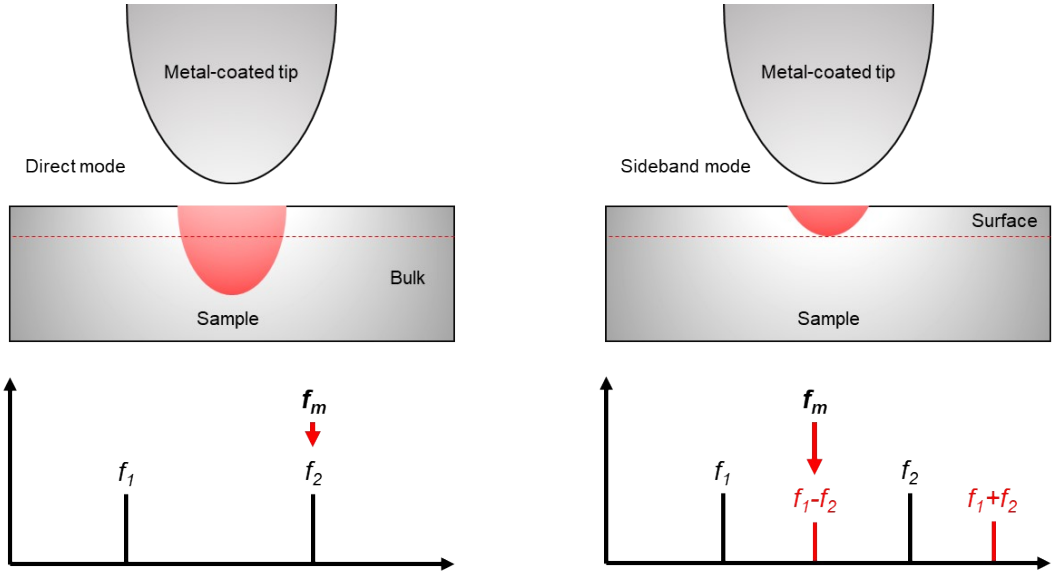

Figure S1. Two different modes of PiFM: direct and sideband mode.

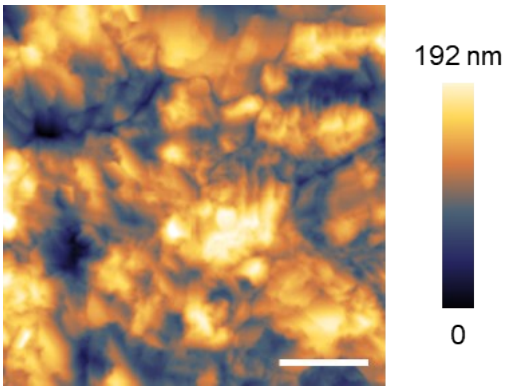

Figure S2. The topography image of pure $FAPbI_3$ perovskite without MACl additive. The scale bar represents 1 μm.

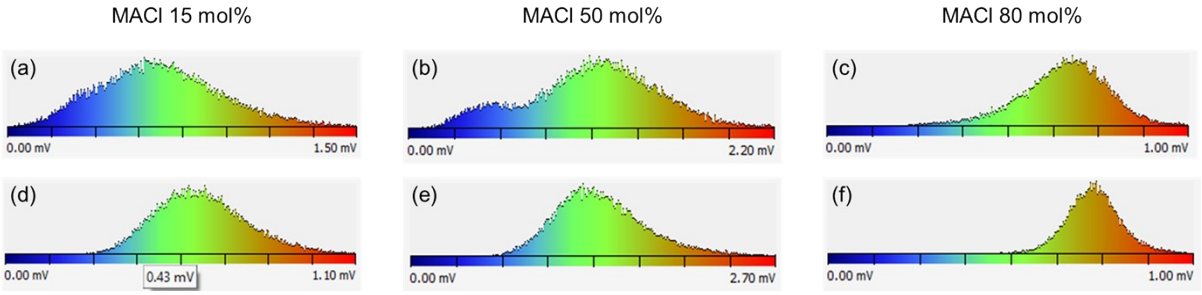

Figure S3. Histogram of FA^+ distribution of $FAPbI_3$ perovskites at (a-c) surface and (d-f) in the bulk region with different mol% of MACl incorporation.

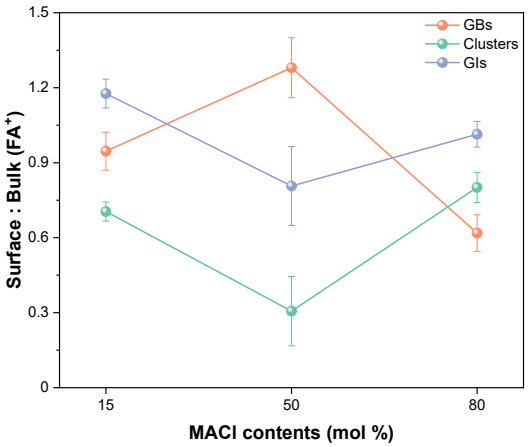

Figure S4. The surface to bulk ratio, calculated from PiFM IR spectra at 1713 cm^{-1} (FA^+) at GBs, clusters and neighbouring grains (GIs) as a function of MACl amount.

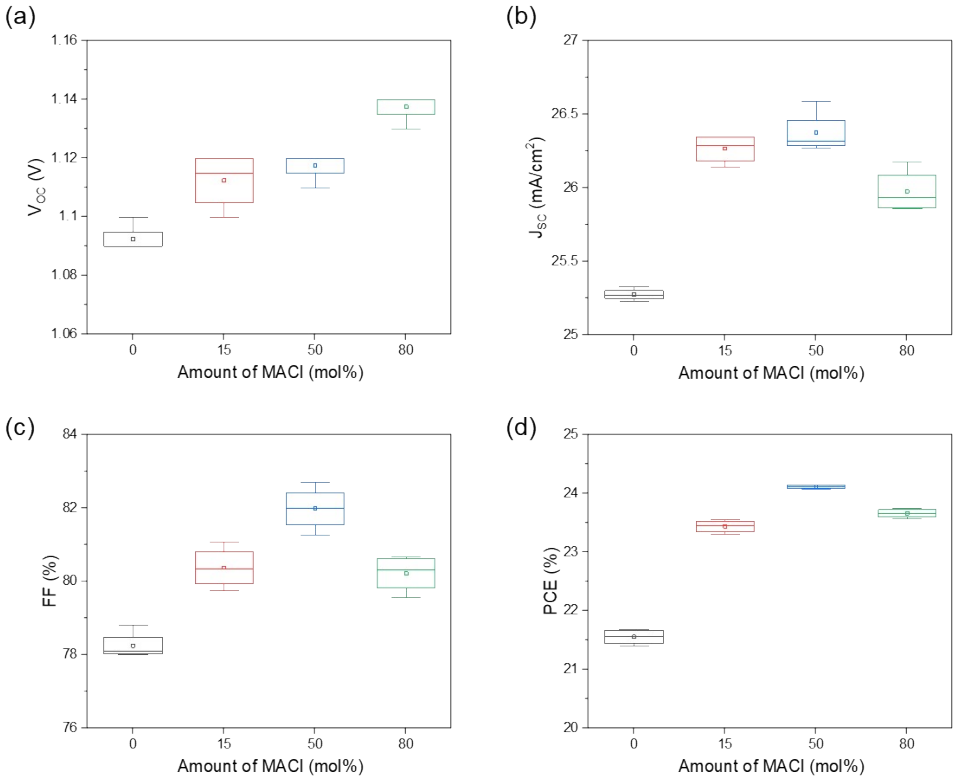

Figure S5. Statistical distribution of the photovoltaic parameters of $FAPbI_3$ perovskite solar cells with different amounts of MACl.

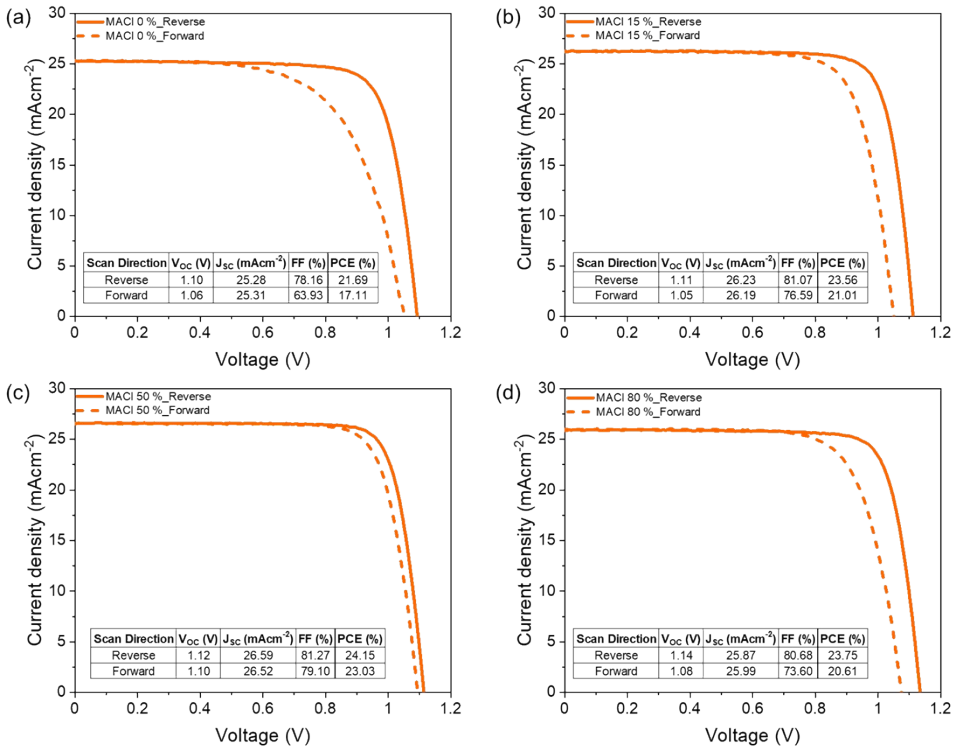

Figure S6. Champion device performance of $FAPbI_3$ perovskite devices with varying the amount of MACl.

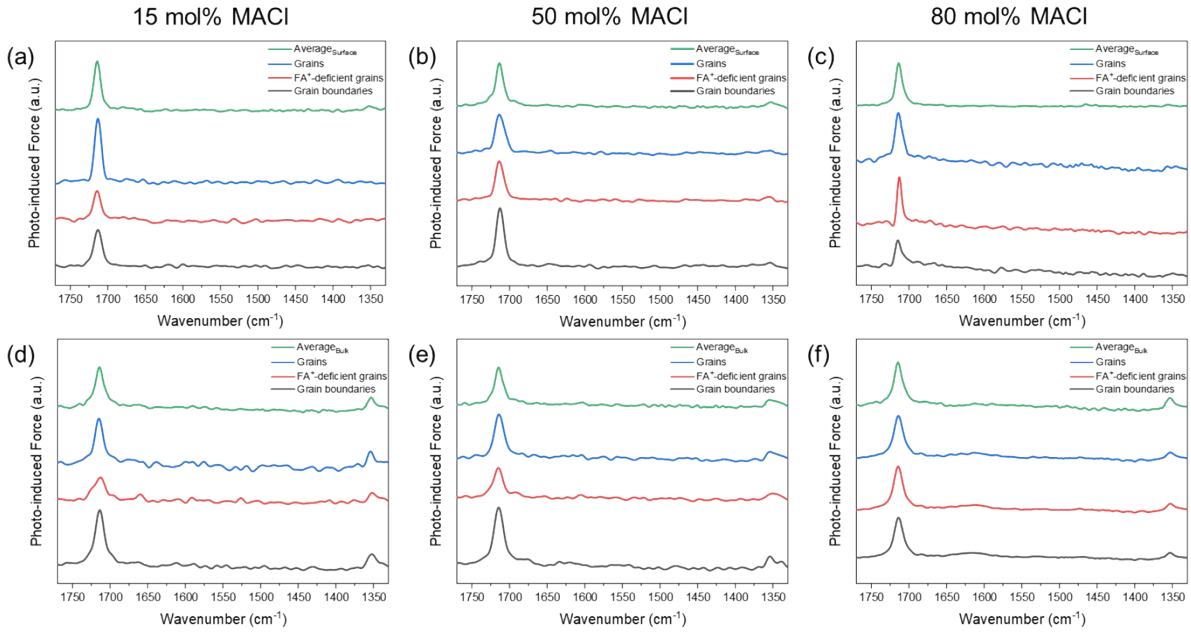

Figure S7. Point IR spectra. (a-c) IR spectra recorded at the surface and (d-f) IR spectra recorded in bulk region, for $FAPbI_3$ perovskites with different amounts of MACl: 15, 50, and 80 mol%, respectively.

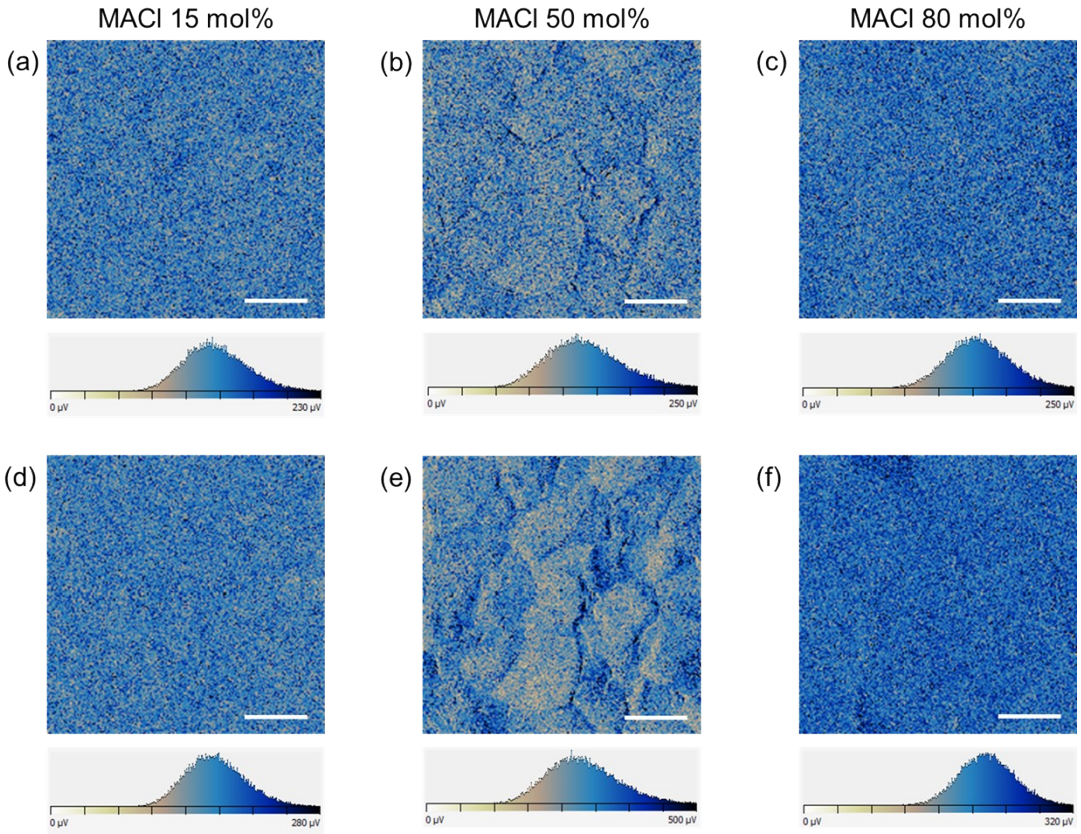

Figure S8. PiFM images at 1465 cm^{-1} (MA^+) of $FAPbI_3$ perovskites with different mol% of MACl incorporation, (a-c) at the surface and (d-f) in bulk region, respectively.

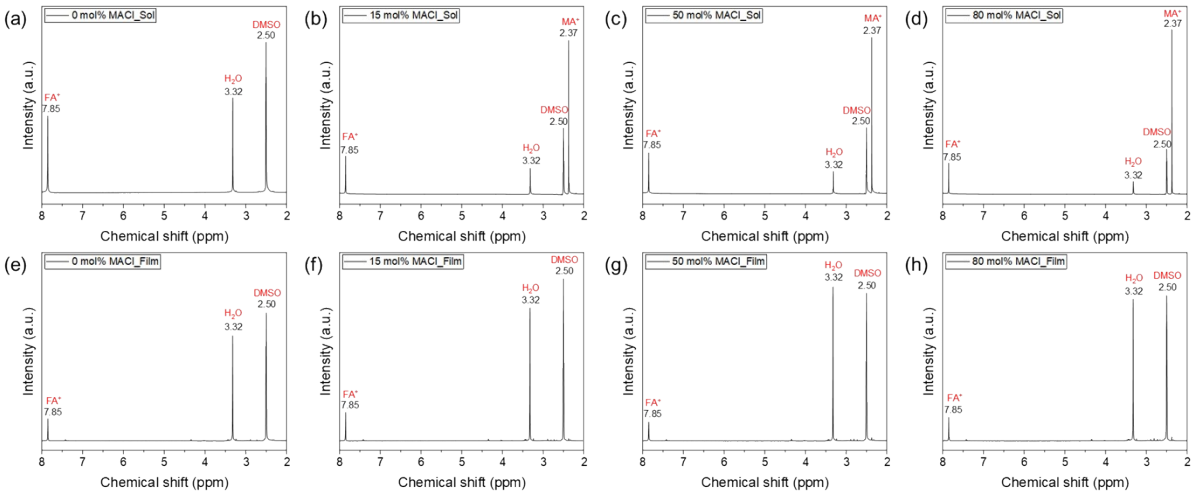

Figure S9. (a-d) ^{1}H-NMR spectra of fresh $FAPbI_3$ perovskite solutions and $FAPbI_3$ perovskite films with different mol% of MACl.

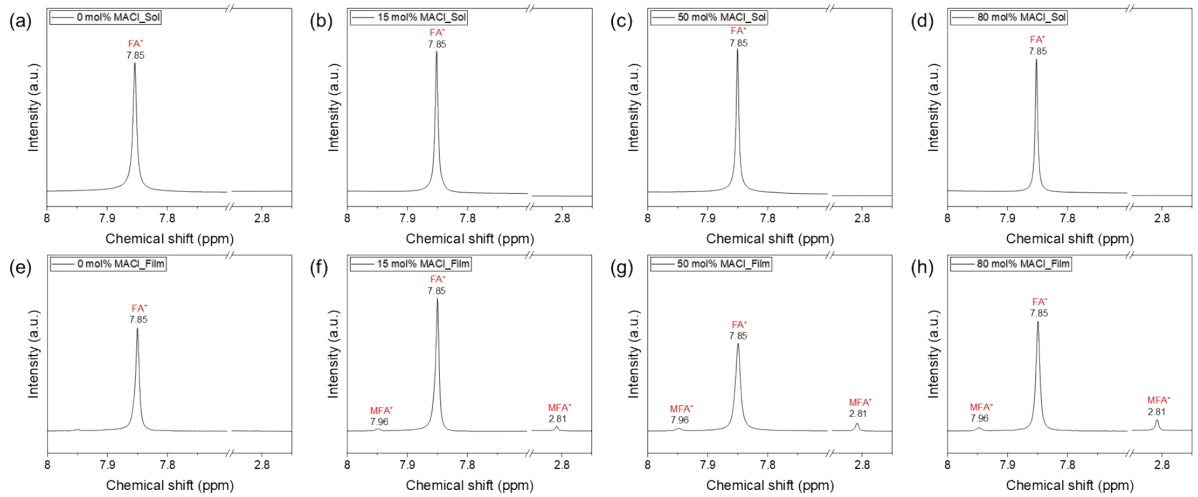

Figure S10. Magnified ^{1}H-NMR spectra for identification of MFA^{+} peaks for fresh $FAPbI_3$ precursor solutions and $FAPbI_3$ perovskite films with different amounts of MACl.

Supplementary Note for **Figures 4:**

4D-STEM data analysis: Automated crystal orientation mapping (ACOM) mapping with a sparse correlation matching method was used[1].

Procedure:

All procedures performed are specified in **Figure S11**. Each panel corresponds to the sequence carried out for the ACOM mapping. Actual examples and notebooks used to analyse the data can be found in the GitHub Repository and Zenodo if further information is required.

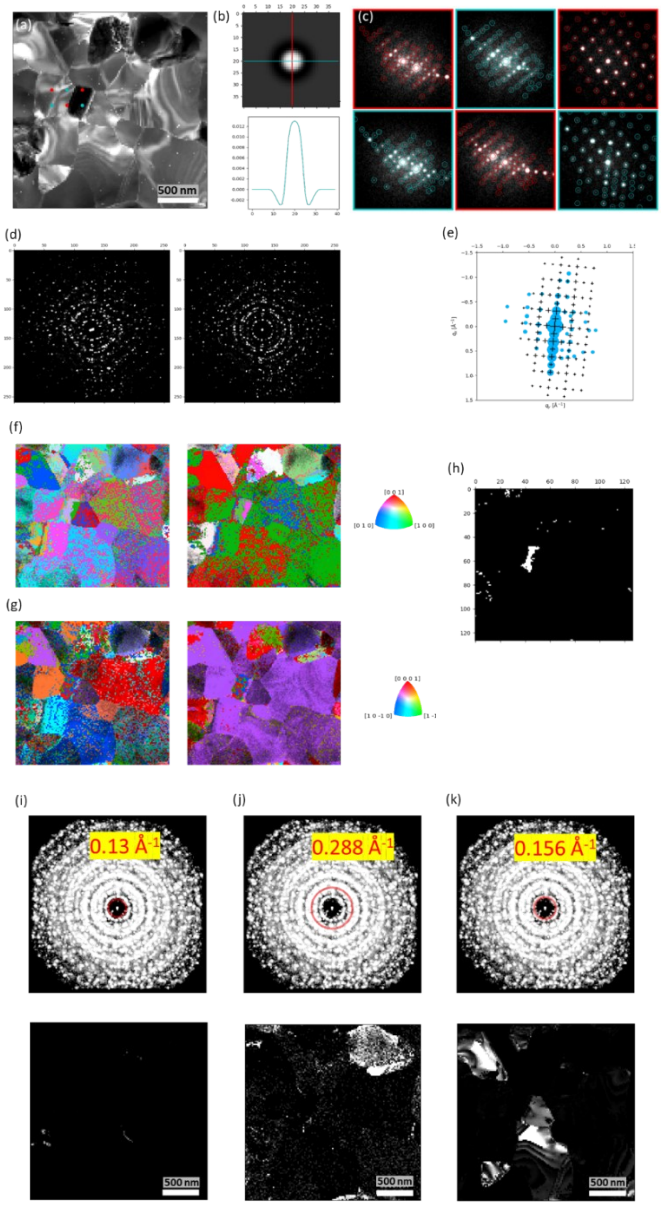

Figure S11. (a) VADF images with some positions selected (for example), (b) Probe kernel used for peak finding, (c) Peak finding outcome for positions highlighted in panel a, (d) All the Bragg vectors before and after alignment, (e) Crystal orientation mapping test with the cubic phase, (f and g) ACOM outcomes for two crystals – cubic $FAPbI_3$ (top), $MFAPbI_3$ (bottom), (h) Regions where confidence in $MFAPbI_3$ phase matching is ~1.2 times for than the cubic $FAPbI_3$. (i, j, and k) VADF integration over the scattering ranges highlighted to map the locations of the $MFAPbI_3$ phase (left, centre) and cubic (right).

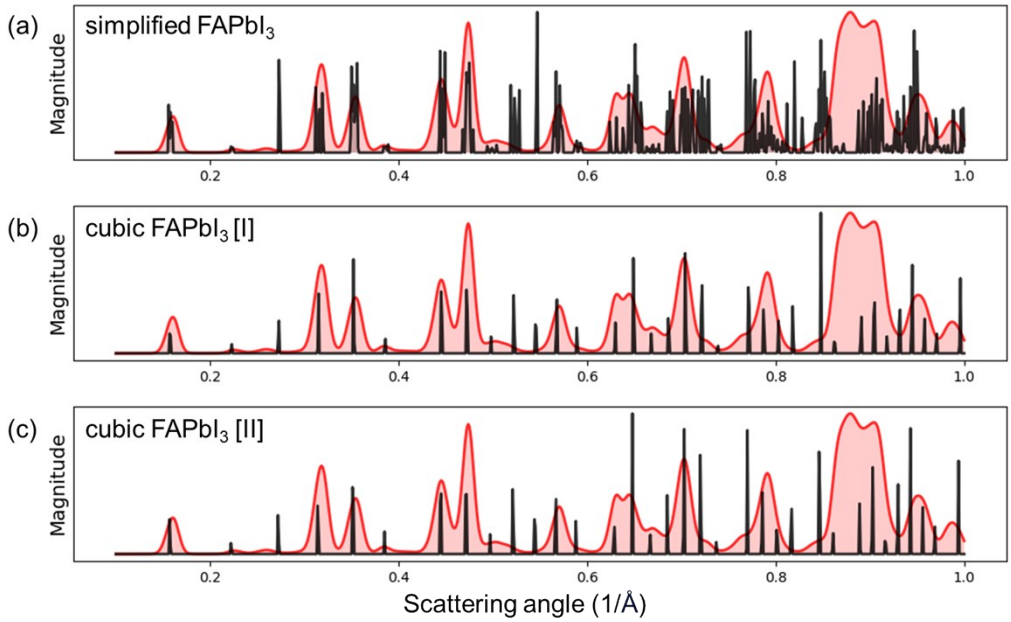

Figure S12. Comparison of the identified peaks in SEND data (in red) with the simulated power diffraction patterns of (a) simplified $FAPbI_3$ phase, (b), and (c) various CIF for cubic $FAPbI_3$ phases from literatures[2,3]. The majority of $FAPbI_3$ perovskite with 50% of MACl can be indexed as pseudo-cubic (close to cubic) $FAPbI_3$ phases.

(a)

Lattice type P
Space group name P 1
Space group number 1
Setting number 1

Lattice parameters

a	b	c	alpha	beta	gamma
6.40746	6.26562	6.33757	90.0000	90.0000	90.0000

Unit-cell volume = 254.432607 Å^3

Structure parameters

			x	y	z	Occ.	B	Site	Sym.
1	C	C1	0.50000	0.52058	0.50000	1.000	1.000	1a	1
2	N	N1	0.68174	0.42573	0.50000	1.000	1.000	1a	1
3	N	N2	0.31826	0.42573	0.50000	1.000	1.000	1a	1
4	H	H1	0.50000	0.69575	0.50000	1.000	1.000	1a	1
5	H	H2	0.81178	0.52048	0.50000	1.000	1.000	1a	1
6	H	H3	0.70197	0.26339	0.50000	1.000	1.000	1a	1
7	H	H4	0.29803	0.26339	0.50000	1.000	1.000	1a	1
8	H	H5	0.18822	0.52048	0.50000	1.000	1.000	1a	1
9	Pb	Pb1	1.00000	0.96593	1.00000	1.000	1.000	1a	1
10	I	I1	0.50000	0.98442	1.00000	1.000	1.000	1a	1
11	I	I2	0.00000	0.46295	1.00000	1.000	1.000	1a	1
12	I	I3	0.00000	0.91970	0.50000	1.000	1.000	1a	1

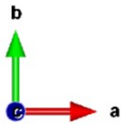

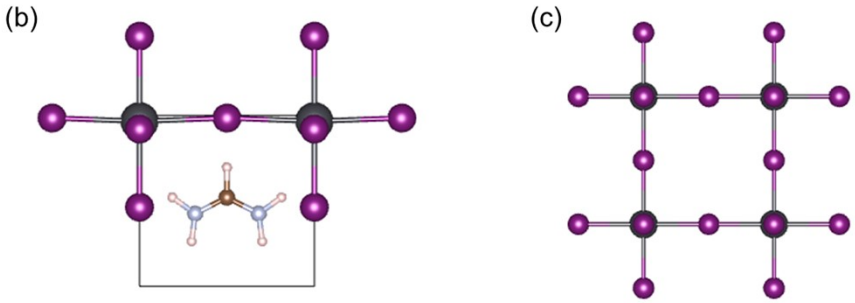

Figure S13. (a) Crystal file of $FAPbI_3$ perovskite used. Simple $FAPbI_3$ perovskite is the simplified version where low e scattering atoms (C, H, N) were removed from (b) the original version, and made (c) pseudo-cubic, to make orientation search in Py4DSTEM more efficient. Note that the complete CIF above was used for comparing sum diffraction patterns with simulations.

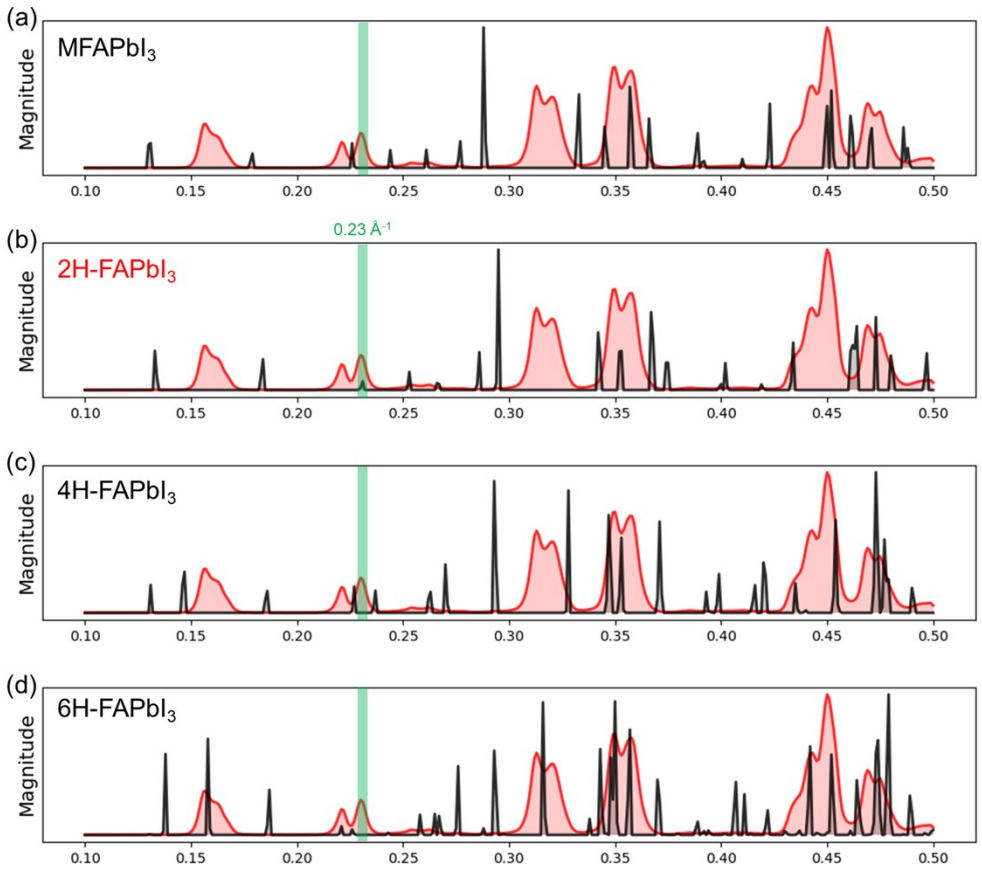

Figure S14. Comparison of the identified peaks in SEND data (in red) with simulated power diffraction patterns of $MFAPbI_3$ phases with different hexagonal polytypes (2H-, 4H-, and 6H-$FAPbI_3$ phases). The peak at 0.23 $Å^{-1}$ corresponds to the 2H-$FAPbI_3$ phase.

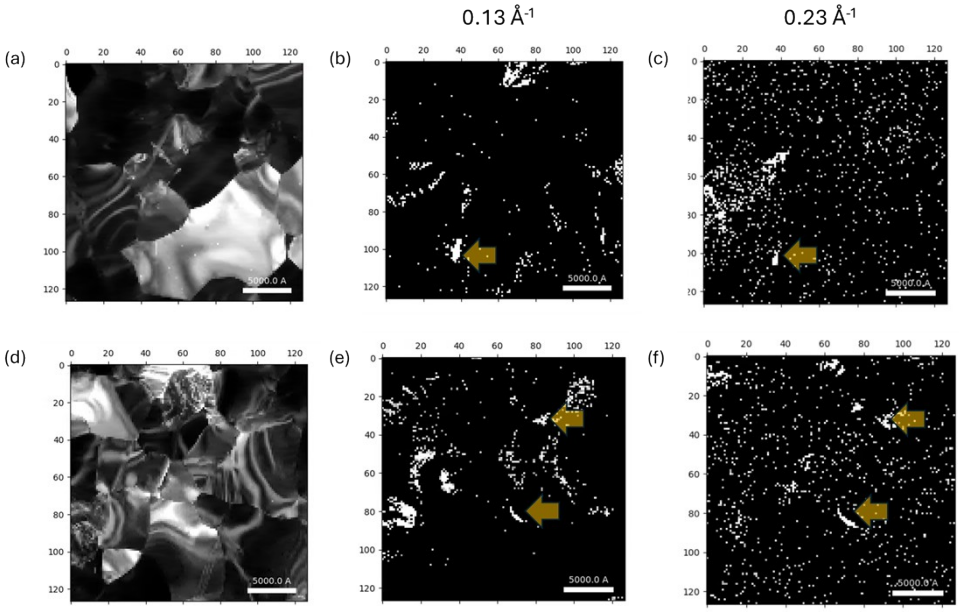

Figure S15. VADF images of two examples SED data with corresponding virtual images: (b, c) and (e, f) using the two different peaks (0.13 $Å^{-1}$ – $MFAPbI_3$ phases, and 0.23 $Å^{-1}$ – 2H-$FAPbI_3$ phases).

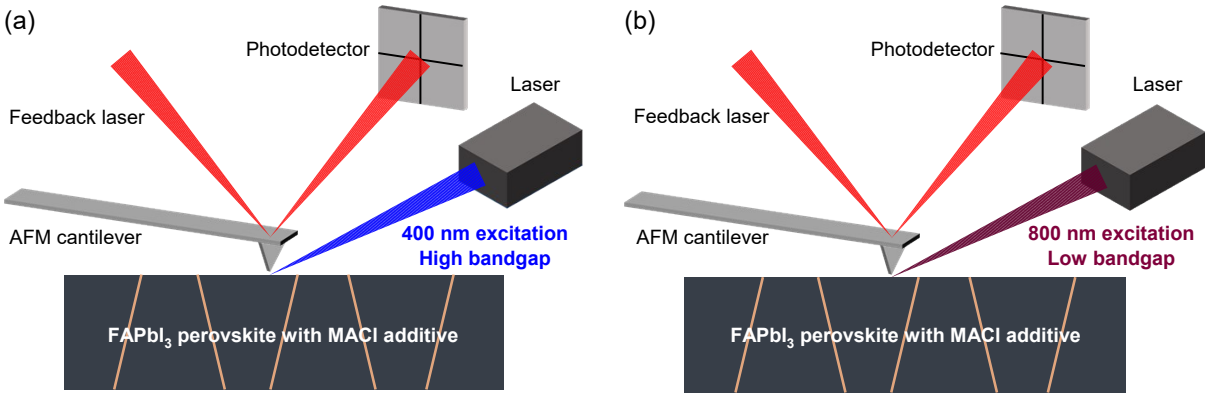

Figure S16. Schematic of wavelength-dependent KPFM measurement, using two different wavelengths of excitation, (a) 400 nm, and (b) 800 nm, which enable to investigate high and low bandgap regions, respectively.

(a)

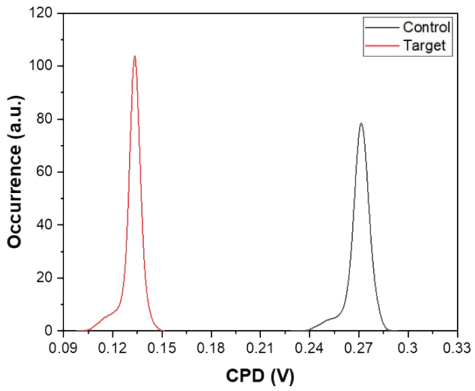

(b)

Perovskite	Minimum (eV)	Peak (eV)	Maximum (eV)
Control	-4.701	**-4.659**	-4.636
Target	-4.832	**-4.797**	-4.778

Figure S17. Average CPD plot of Control (pure $FAPbI_3$) perovskite and Target ($FAPbI_3$ perovskite with the optimal amount of MACl) acquired in dark condition, and (b) Summary of the calculated work function of each sample.

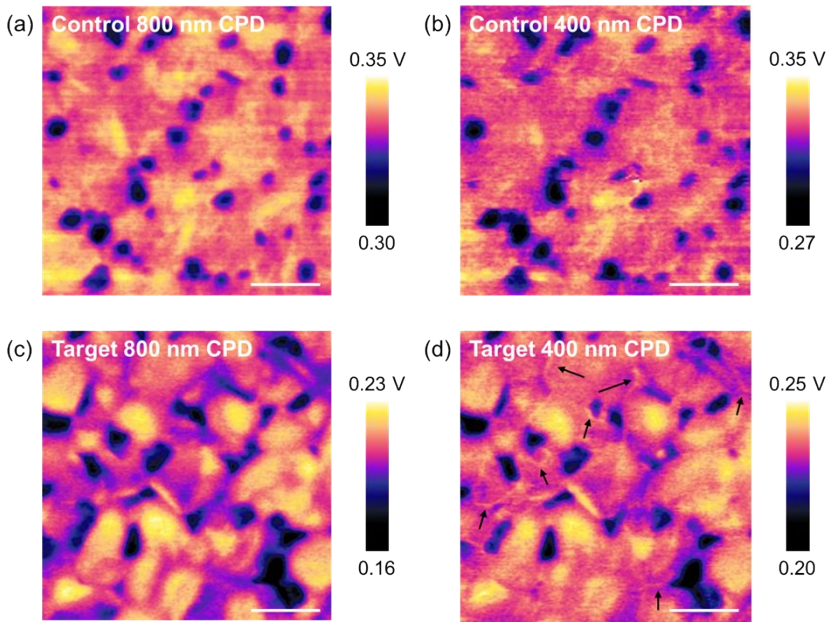

Figure S18. (a-b) CPD spatial maps of Control film and (c-d) Target film measured under illumination using 800, and 400 nm laser excitation, respectively. Black arrows in panel (d) indicate brighter contrast at the GBs compared to neighbouring grains. The scale bar represents 1 μm.

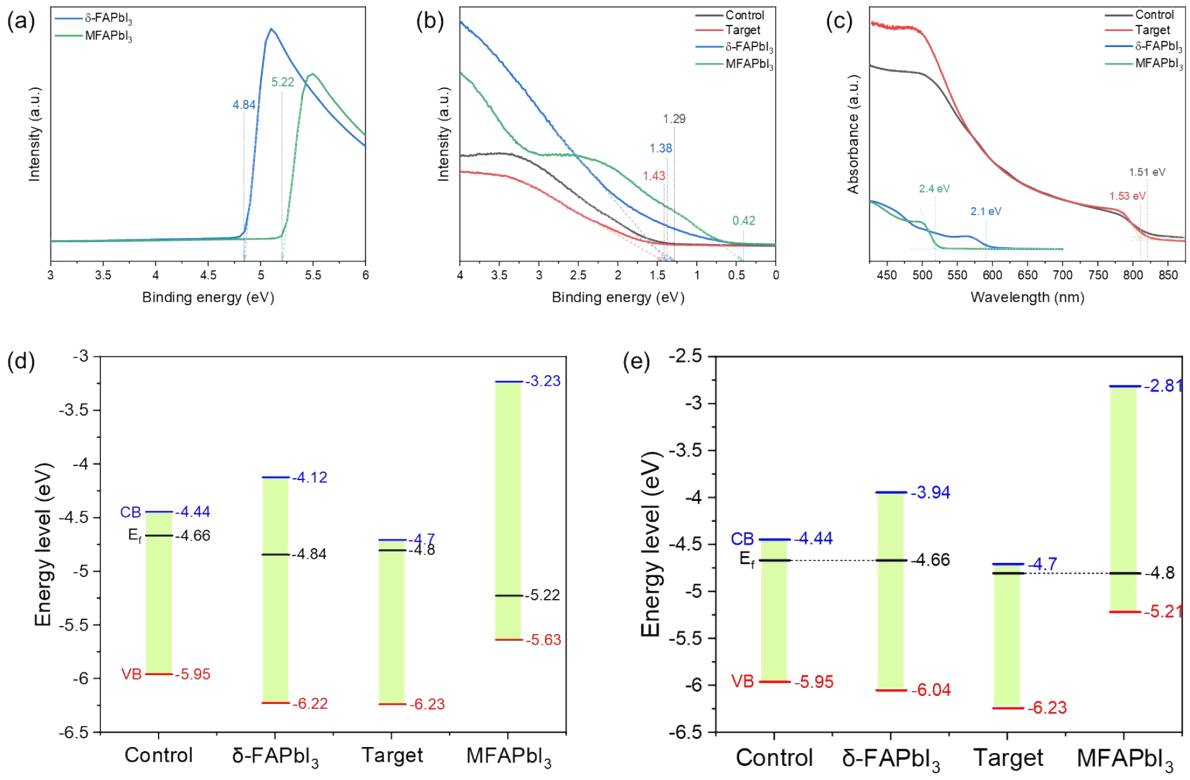

Figure S19. UPS measurements. (a) UPS spectra around the secondary electron cut-off, (b) UPS spectra in the valence band (VB) region, (c) absorption curves of Control, Target, δ-$FAPbI_3$, and $MFAPbI_3$ perovskite films, (d) energy level diagram and (e) energy level diagram of δ-$FAPbI_3$ and $MFAPbI_3$ aligned with fermi level of Control and Target perovskite films, respectively. Note that work function values of Control and Target perovskite film are extracted from KPFM measurement in **Figure S17**.

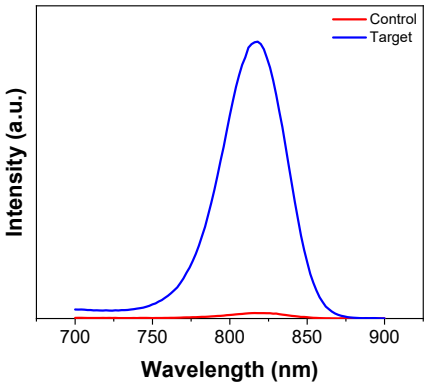

Figure S20. Steady-state spectral PL measurements of Control ($FAPbI_3$ with 0% MACl) and Target ($FAPbI_3$ with 50% MACl) perovskite films.

Table S1. Calculated molar fractions of A-site cations for increasing the amount of MACl, calculated from **Figure S5**.

MACl concentration	MA^+ [%]	MFA^+ [%]	FA^+ [%]
0 mol%	0	0	100
15 mol%	3.56	0.31	96.13
50 mol%	4.42	1.60	93.98
80 mol%	4.72	0.94	94.34

Reference

1 C. Ophus, S. E. Zeltmann, A. Bruefach, A. Rakowski, B. H. Savitzky, A. M. Minor and M. C. Scott, *Microscopy and Microanalysis*, 2022, **28**, 390–403.

2 P. Gratia, I. Zimmermann, P. Schouwink, J.-H. Yum, J.-N. Audinot, K. Sivula, T. Wirtz and M. K. Nazeeruddin, *ACS Energy Lett*, 2017, **2**, 2686–2693.

3 T. A. S. Doherty, A. J. Winchester, S. Macpherson, D. N. Johnstone, V. Pareek, E. M. Tennyson, S. Kosar, F. U. Kosasih, M. Anaya, M. Abdi-Jalebi, Z. Andaji-Garmaroudi, E. L. Wong, J. Madéo, Y.-H. Chiang, J.-S. Park, Y.-K. Jung, C. E. Petoukhoff, G. Divitini, M. K. L. Man, C. Ducati, A. Walsh, P. A. Midgley, K. M. Dani and S. D. Stranks, *Nature*, 2020, **580**, 360–366.